

Rossby wave instability in weakly ionized protoplanetary disks. I. azimuthal or vertical B-fields

Can Cui^{1,2*}, Ashutosh Tripathi², Cong Yu^{3,4}, Min-Kai Lin^{5,6} and Andrew Youdin^{7,8}

¹*Department of Astronomy and Astrophysics, University of Toronto, Toronto, ON M5S 3H4, Canada*

²*DAMTP, University of Cambridge, Wilberforce Road, Cambridge CB3 0WA, UK*

³*School of Physics and Astronomy, Sun Yat-Sen University, Zhuhai 519082, China*

⁴*CSST Science Center for the Guangdong-Hong Kong-Macau Greater Bay Area, Zhuhai 519082, China*

⁵*Institute of Astronomy and Astrophysics, Academia Sinica, Taipei 10617, Taiwan, R.O.C.*

⁶*Physics Division, National Center for Theoretical Sciences, Taipei 10617, Taiwan, R.O.C.*

⁷*Department of Astronomy and Steward Observatory, University of Arizona, Tucson, AZ 85721, USA*

⁸*The Lunar and Planetary Laboratory, University of Arizona, Tucson, AZ 85721, USA*

3 July 2024

ABSTRACT

Rossby wave instability (RWI) is considered the underlying mechanism to crescent-shaped azimuthal asymmetries, discovered in (sub-)millimeter dust continuum of many protoplanetary disks. Previous works on linear theory were conducted in the hydrodynamic limit. Nevertheless, protoplanetary disks are likely magnetized and weakly ionized. We examine the influence of magnetic fields and non-ideal magnetohydrodynamic (MHD) effects - namely, Ohmic resistivity, Hall drift, and ambipolar diffusion - on the RWI unstable modes. We perform radially global linear analyses, employing constant azimuthal (B_ϕ) or vertical (B_z) background magnetic fields. It is found that, in the ideal MHD regime, magnetism can either enhance or diminish RWI growth. Strong non-ideal MHD effects cause RWI growth rates to recover hydrodynamic results. The sign of Hall Elsässer number subtly complicates the results, and vertical wavenumbers generically diminish growth rates.

Key words: hydrodynamics – MHD – methods: analytical – protoplanetary disks

1 INTRODUCTION

Protoplanetary disks are composed of gas and dust orbiting pre-main-sequence stars (Armitage 2011). They are the birth place of planets, where micron-sized dust grains coalesce and evolve into km-sized planetesimals, eventually giving rise to terrestrial planets or gas giants cores. Nevertheless, the growth of dust grains faces several barriers, including bouncing, fragmentation, and fast radial drift (Weidenschilling 1977; Güttler et al. 2010; Zsom et al. 2010). Rossby wave instability (RWI) is perhaps a promising mechanism to circumvent these barriers. Its non-linear state generates large, lopsided crescent-shaped vortices, which concentrate grains towards pressure maximum, fostering streaming instability and subsequent gravitational collapse (Goldreich & Ward 1973; Youdin & Goodman 2005). These vortices manifest as azimuthal asymmetries observed in (sub-)millimeter dust continuum as well as CO rotational transition lines (e.g., Huang et al. 2018; van der Marel et al. 2021). Notable exam-

ples include IRS 48 (van der Marel et al. 2013), HD142527 (Muto et al. 2015), and AB Aur (Fuente et al. 2017).

The RWI is triggered by local extrema in the radial profile of vortensity, $(\Sigma\Omega/\kappa^2)S^{2/\Gamma}$ (Lovelace et al. 1999; Li et al. 2000). It gives exponential growth of non-axisymmetric modes ($\propto \exp[im\phi]$, where $m = 1, 2, \dots$) on each side of the corotation radius. These unstable Rossby modes are confined between the inner and outer Lindblad resonances, where density waves are launched and propagate away from the resonances (Lin & Shu 1964; Tsang & Lai 2008). The eigenfunctions of Rossby waves manifest as anticyclonic vortices, characterized by vorticity ($\nabla \times \delta\mathbf{u}$) directed oppositely to the rotation of the disk, yielding a maximum perturbed pressure at the vortex core (Lovelace & Romanova 2014). Extensions of the classic RWI incorporating self-gravity (Lin & Papaloizou 2011; Lin 2012), magnetic fields (Yu & Li 2009; Yu & Lai 2013), and dust-gas two-fluid drag (Liu & Bai 2023) have been explored.

In the context of protoplanetary disks, numerical simulations of the RWI have been commonly performed at the gap edges carved by a planet (Zhu et al. 2014;

* can.cui@astro.utoronto.ca

Zhu & Stone 2014; Hammer et al. 2017; Huang et al. 2018; Cimerman & Rafikov 2023), or at the dead zone edges of the magneto-rotational instability (MRI; Lyra & Mac Low 2012; Miranda et al. 2016, 2017), for which local vortensity extrema take place. These simulations elucidate that the non-linear saturation of the Rossby vortices is primarily governed by $m = 1$ modes (Godon & Livio 1999; Li et al. 2001; Meheut et al. 2012). Furthermore, the long-term survival of Rossby vortices are examined under secondary instabilities (e.g., Lesur & Papaloizou 2009), thermal relaxation (e.g., Fung & Ono 2021; Rometsch et al. 2021), and dust-gas two-fluid framework (e.g., Surville et al. 2016; Surville & Mayer 2019; Li et al. 2020).

While the RWI is inherently a hydrodynamic phenomenon, it is crucial to acknowledge the magnetized nature of protoplanetary disks, where magnetic fields likely originate from primordial molecular clouds (Galli & Shu 1993; Girart et al. 2006, 2009). Owing to the weak thermal ionization of passively heated protoplanetary disks and the modest non-thermal ionization by, for instance, the stellar FUV, EUV, X-rays, and cosmic rays (Wardle 2007; Bai 2011), the gas and magnetic fields are not perfectly coupled. The disk material may be weakly ionized, and three non-ideal MHD effects come into play: Ohmic resistivity, the Hall drift, and ambipolar diffusion (Weiss et al. 2021; Lesur 2021). At the same ionization fraction, Ohmic, Hall, and ambipolar diffusivities are respectively proportional to $\eta_{\text{O}} \propto \text{const.}$, $\eta_{\text{H}} \propto B/\rho$, and $\eta_{\text{A}} \propto B^2/\rho^2$. Consequently, Ohmic resistivity dominates in high-density regions near the inner disk and at the mid-plane, while ambipolar diffusion becomes prominent in the outer disk. Hall drift is most effective between these regions. Both numerical simulations and analytical theory have underscored the significance of non-ideal MHD effects in shaping disk structure and evolution, such as dead zone structures (e.g., Flock et al. 2017), magnetized wind kinematics (e.g., Wang et al. 2019), dust dynamics and distribution (e.g., Lin & Hsu 2022; Wu et al. 2024), heating and disk temperature profiles (e.g., Béthune & Latter 2020), and the formation of annular substructures (e.g., Riols & Lesur 2019; Cui & Bai 2021, 2022).

Previously, the non-ideal MHD effects were incorporated in the linear studies of several instabilities applicable to protoplanetary disks, for example, the MRI (Balbus & Hawley 1991) and the vertical shear instability (Goldreich & Schubert 1967; Nelson et al. 2013). These investigations unveiled significant alterations in the unstable modes induced by non-ideal MHD physics. In the context of MRI, both Ohmic resistivity and ambipolar diffusion tend to stabilize the instability, although under specific conditions, ambipolar diffusion shear instability can be excited (Blaes & Balbus 1994; Kunz & Balbus 2004; Latter & Kunz 2022). The impact of Hall drift is twofold, based upon the sign of the Hall Elsässer number (Wardle 1999; Pandey & Wardle 2012). Concerning the vertical shear instability, strong ionization can substantially weaken the unstable modes, while subdued modes regain strength under weak ionizations (Latter & Papaloizou 2018; Cui & Bai 2020; Cui & Lin 2021; Latter & Kunz 2022).

To deepen our comprehension of RWI behavior in magnetized disks, investigations must encompass both ideal and non-ideal MHD physics. Previous studies have primarily focused on the ideal MHD regime. Yu & Li (2009) utilized

Lagrangian perturbation theory to probe the influence of toroidal magnetic fields on the RWI. Their findings revealed a continuous reduction in growth rates with increasing magnetization. Subsequently, Yu & Lai (2013) explored the impact of poloidal fields using a vertically integrated disk model. Interestingly, they observed a dichotomy in results: pure vertical fields typically diminish RWI growth rates, whereas the presence of radial fields tends to enhance them.

In this work, we explore the RWI unstable modes in the ideal and non-ideal MHD limit, employing three-dimensional linear analysis with Eulerian perturbations. The paper is organized as follows. In Section 2, we introduce the governing dynamical equations and the perturbation equations that delineate our theoretical framework. Section 3 elaborates on the numerical methodologies employed to solve the set of ordinary differential equations (ODEs) governing the magnetized RWI. In Section 4, we present numerical solutions obtained and elucidate the observed RWI behaviors. We summarize the main findings in Section 5 and compare the RWI linear growth to MRI in Section 6.

2 THEORY

2.1 Dynamical equations

The stability of a three-dimensional, thin, magnetized disk with background radial vortensity extrema is analyzed in cylindrical coordinates (r, ϕ, z) . The gravitational potential is given by $\Phi = -GM_*/(r^2 + z^2)^{1/2}$, where M_* is the mass of central star. Disk self-gravity is neglected. The governing equations for this compressible, magnetized disk in Gaussian units are the continuity, momentum, and entropy conservation equations,

$$\frac{d\rho}{dt} + \rho \nabla \cdot \mathbf{v} = 0, \quad (1)$$

$$\frac{d\mathbf{v}}{dt} + \frac{1}{\rho} \nabla \left[P + \frac{B^2}{8\pi} \right] + \nabla \Phi - \frac{1}{4\pi\rho} (\mathbf{B} \cdot \nabla) \mathbf{B} = 0, \quad (2)$$

$$\frac{dS}{dt} = 0, \quad (3)$$

where the material derivative is defined as $d/dt \equiv \partial/\partial t + \mathbf{v} \cdot \nabla$, and $S \equiv P/\rho^{\Gamma}$ is the entropy of the disk matter. The induction equation is written as,

$$\frac{\partial \mathbf{B}}{\partial t} - \nabla \times (\mathbf{v} \times \mathbf{B} - c\mathbf{E}') = 0. \quad (4)$$

The non-ideal MHD terms manifest in the electric field of the rest fluid frame,

$$\mathbf{E}' = \frac{4\pi}{c^2} [\eta_{\text{O}} \mathbf{J} + \eta_{\text{H}} \mathbf{J} \times \mathbf{b} - \eta_{\text{A}} (\mathbf{J} \times \mathbf{b}) \times \mathbf{b}], \quad (5)$$

where the unit vector of magnetic field is denoted by $\mathbf{b} = \mathbf{B}/|B|$, and Ohmic, Hall, ambipolar diffusivities are denoted by η_{O} , η_{H} , and η_{A} , respectively. The current density is $\mathbf{J} = c\nabla \times \mathbf{B}/4\pi$. Using the divergence free condition $\nabla \cdot \mathbf{B} = 0$, the induction equation can be cast into

$$\frac{d\mathbf{B}}{dt} - (\mathbf{B} \cdot \nabla) \mathbf{v} + (\nabla \cdot \mathbf{v}) \mathbf{B} + c\nabla \times \mathbf{E}' = 0. \quad (6)$$

2.2 Equilibrium of the disk

The equilibrium disk model is stationary ($\partial/\partial t = 0$), axisymmetric ($\partial/\partial\phi = 0$), and radially global. All background quantities are independent of z . The steady-state physical quantities are denoted by the subscript “0”. The equilibrium velocity field has only the azimuthal component, $v_{\phi 0} = \Omega_0 r$.

The necessary condition for Rossby wave instability is the presence of radial vortensity extrema. This can be achieved by setting up a Gaussian bump centered at $r = r_0$ in the density profile (e.g., Li et al. 2000),

$$\frac{\rho_0}{\rho_{00}} = 1 + (A - 1) \exp \left[-\frac{1}{2} \left(\frac{r - r_0}{\Delta r} \right)^2 \right], \quad (7)$$

where ρ_{00} is the background density profile without the Gaussian bump. Despite of the radially global nature of the disk model, ρ_{00} is taken to be a constant for simplicity. Setting it to a power-law distribution will not qualitatively alter the results as noted in Li et al. (2000).

To compute the background pressure P_0 , we consider a barotropic flow, and hence the pressure is only a function of density $P_0(\rho_0)$, expressed by

$$\frac{P_0}{P_{0*}} = \left[\frac{\rho_0}{\rho_{0*}} \right]^\Gamma, \quad (8)$$

where subscript “0*” denotes background quantities evaluated at r_0 , and Γ is the adiabatic index. The adiabatic sound speed is defined as $c_{s0} \equiv (\Gamma P_0/\rho_0)^{1/2}$. By specifying c_{s0*} , we can obtain P_{0*} and subsequently P_0 . Throughout the paper, we set $GM = \rho_0 = r_0 = 1$, $\Delta r/r_0 = 0.05$, $\Gamma = 5/3$, $A = 1.5$, and the disk aspect ratio $c_{s0*}/v_{\phi 0*} = 0.06$ at r_0 . The pressure scale height $H \approx c_{s0*}/\Omega_{K0*}$, where Ω_{K0*} is the Keplerian angular speed at r_0 .

We construct a simplified equilibrium solution for this study, setting \mathbf{B}_0 a constant vector. In equilibrium, the radial momentum equation gives

$$\frac{v_{\phi 0}^2(r, z)}{r} = \frac{1}{\rho_0} \frac{\partial P_0(r)}{\partial r} + \frac{\partial \Phi(r, z)}{\partial r}. \quad (9)$$

In the ideal MHD limit, the ϕ -component of induction equation is

$$\left[B_{r0} \frac{\partial}{\partial r} + B_{z0} \frac{\partial}{\partial z} - \frac{B_{r0}}{r} \right] v_{\phi 0} = 0. \quad (10)$$

It is immediately seen that $B_{\phi 0}$ is not involved in these equations, and hence is free to specify. By thin disk approximations, $\Phi(r, z) \approx \Phi(r) = -GM_*/r$, and $v_{\phi 0}(r, z) \approx v_{\phi 0}(r)$. Then for $B_{r0} = 0$, we are completely free to specify B_{z0} , and the constant equilibrium magnetic field is taken to be $\mathbf{B}_0 = (0, B_{\phi 0}, B_{z0})$.

When considering non-ideal MHD physics to equilibrium solutions, only the induction equation (4) is modified. The current density \mathbf{J} vanishes for a pure B_z field, and eq (10) is strictly satisfied. However, the existence of curvature terms from cylindrical coordinates render non-zero $\nabla \times c\mathbf{E}'$ for a pure B_ϕ field. Hence, our equilibrium magnetic field is only valid if we ignore the curvature terms in curl operator.

The strengths of $B_{\phi 0}$ and B_{z0} are parameterized by plasma β , defined as the ratio of gas pressure to magnetic pressure,

$$\beta = \frac{8\pi P_0}{B_0^2}, \quad (11)$$

and $\beta > 1$ is commonly satisfied in protoplanetary disks.

Finally, we quantify the strength of non-ideal MHD effects by their respective Elsässer numbers,

$$\Lambda = \frac{v_A^2}{\eta_0 \Omega_K}, \quad (12)$$

$$\text{Ha} = \frac{v_A^2}{\eta_H \Omega_K}, \quad (13)$$

$$\text{Am} = \frac{v_A^2}{\eta_\Lambda \Omega_K}, \quad (14)$$

where the Alfvén velocity is $v_A^2 = B_0^2/4\pi\rho_0$, and Ω_K is the Keplerian angular speed.

2.3 Perturbations of the disk

Consider small perturbations to eqs (1)-(4), such that $\mathbf{v} = \mathbf{v}_0 + \delta\mathbf{v}(r, z, \phi, t)$, $\mathbf{B} = \mathbf{B}_0 + \delta\mathbf{B}(r, z, \phi, t)$, ..., . We linearize these equations by considering Eulerian perturbations $\propto f(r) \exp(ik_z z + im\phi - i\omega t)$, where k_z is the vertical wavenumber, m is the azimuthal mode number, and $\omega = \omega_r + i\gamma$ is the mode frequency, where γ denotes the growth rate. We further define the Doppler-shifted wave frequency $\Delta\omega = \omega - m\Omega$, the azimuthal wavenumber $k_\phi = m/r$, and the radial epicyclic frequency $\kappa = [r^{-3} d(r^4 \Omega^2)/dr]^{1/2}$.

We now drop subscript “0” for the background quantities throughout rest of the paper. Our model encompasses eight perturbed quantities, $\delta\mathbf{v}$, $\delta\mathbf{B}$, $\delta\rho$, $\delta\Psi$, where

$$\delta\Psi = \frac{\delta P}{\rho}, \quad (15)$$

and

$$\frac{\partial \delta\Psi}{\partial r} = \frac{1}{\rho} \frac{\partial \delta P}{\partial r} - \frac{1}{\rho} \frac{\partial \delta\rho}{\partial r} \delta\Psi. \quad (16)$$

We follow Lovelace et al. (1999)’s and Li et al. (2000)’s original paper, and define radial length scales of entropy, pressure, and density variations as

$$L_S \equiv \frac{\Gamma}{d \ln S / dr}, \quad (17)$$

$$L_P \equiv \frac{\Gamma}{d \ln P / dr}, \quad (18)$$

$$L_\rho \equiv \frac{1}{d \ln \rho / dr}. \quad (19)$$

These length scales are related by

$$\frac{1}{L_P} = \frac{1}{L_S} + \frac{1}{L_\rho}. \quad (20)$$

For a barotropic flow, the length scale of entropy approaches infinity, $1/L_S \rightarrow 0$.

To present the perturbation equations optimally, we separate them into two cases: $k_z = 0$ (§2.3) and $k_z \neq 0$ (Appendix A). We first show the set of linearized equations in the ideal MHD limit. In the non-ideal MHD limit, we split the equations into pure vertical and toroidal magnetic field regimes.

2.3.1 ideal MHD

We first derive the linearized equations in the ideal MHD limit. For continuity equation (1) it is

$$\frac{\partial \delta v_r}{\partial r} + \left[\frac{1}{r} + \frac{1}{L_\rho} \right] \delta v_r + ik_\phi \delta v_\phi - i\Delta\omega \frac{\delta \Psi}{c_s^2} = 0. \quad (21)$$

The linearized momentum equations (2) are

$$\begin{aligned} i\Delta\omega \delta v_r + 2\Omega \delta v_\phi - \frac{\partial \delta \Psi}{\partial r} \\ + \frac{1}{4\pi\rho} \left[ik_\phi B_\phi \delta B_r - \frac{2B_\phi}{r} \delta B_\phi - B_z \frac{\delta B_z}{\partial r} - B_\phi \frac{\delta B_\phi}{\partial r} + \frac{B_\phi^2}{r} \frac{\delta \rho}{\rho} \right] \\ = 0, \end{aligned} \quad (22)$$

$$i\Delta\omega \delta v_\phi - \frac{\kappa^2}{2\Omega} \delta v_r - ik_\phi \delta \Psi + \frac{1}{4\pi\rho} \left[\frac{B_\phi}{r} \delta B_r - ik_\phi B_z \delta B_z \right] = 0, \quad (23)$$

$$i\Delta\omega \delta v_z + \frac{ik_\phi B_\phi}{4\pi\rho} \delta B_z = 0. \quad (24)$$

The linearized induction equations (4) are

$$i\Delta\omega \delta B_r + ik_\phi B_\phi \delta v_r = 0, \quad (25)$$

$$i\Delta\omega \delta B_\phi + \left[\frac{\partial v_\phi}{\partial r} - \frac{v_\phi}{r} \right] \delta B_r - B_\phi \frac{\partial \delta v_r}{\partial r} = 0, \quad (26)$$

$$i\Delta\omega \delta B_z - \frac{B_z}{r} \delta v_r - ik_\phi B_z \delta v_\phi + ik_\phi B_\phi \delta v_z - B_z \frac{\partial \delta v_r}{\partial r} = 0. \quad (27)$$

Lastly, the entropy conservation (3) yields

$$i\Delta\omega \frac{\delta P}{P} - i\Delta\omega \Gamma \frac{\delta \rho}{\rho} - \frac{\Gamma}{L_S} \delta v_r = 0. \quad (28)$$

The barotropic assumption gives $1/L_S \rightarrow 0$, and eq (28) simplifies to

$$\delta \Psi = c_s^2 \frac{\delta \rho}{\rho}. \quad (29)$$

It is the barotropic fluid assumption that transforms the set of perturbation equations into standard eigenvalue problems (see §3). According to eq (15), it is straightforward to see that the perturbed pressure is related to density by $\delta P = c_s^2 \delta \rho$.

2.3.2 non-ideal MHD limit: pure B_ϕ

When non-ideal MHD effects apply, the continuity and entropy equations (eqs (21) and (29)) remain unchanged, while the other equations are modified. We now express the linearized equations for pure B_ϕ . The perturbed momentum equations are

$$\begin{aligned} i\Delta\omega \delta v_r + 2\Omega \delta v_\phi - \frac{\partial \delta \Psi}{\partial r} \\ + \frac{1}{4\pi\rho} \left[ik_\phi B_\phi \delta B_r - \frac{2B_\phi}{r} \delta B_\phi - B_\phi \frac{\partial \delta B_\phi}{\partial r} + \frac{B_\phi^2}{r} \frac{\delta \rho}{\rho} \right] \\ = 0, \end{aligned} \quad (30)$$

$$i\Delta\omega \delta v_\phi - \frac{\kappa^2}{2\Omega} \delta v_r - ik_\phi \delta \Psi + \frac{1}{4\pi\rho} \left[\frac{B_\phi}{r} \delta B_r \right] = 0, \quad (31)$$

$$i\Delta\omega \delta v_z + \frac{ik_\phi B_\phi}{4\pi\rho} \delta B_z = 0. \quad (32)$$

The perturbed induction equations are

$$\begin{aligned} i\Delta\omega \delta B_r + ik_\phi B_\phi \delta v_r \\ + [\eta_O + \eta_A] \left[\frac{\partial^2 \delta B_r}{\partial r^2} + \frac{1}{r} \frac{\partial \delta B_r}{\partial r} - k_\phi^2 \delta B_r - \frac{\delta B_r}{r^2} - \frac{2}{r} ik_\phi \delta B_\phi \right] \\ + \eta_H [k_\phi^2 \delta B_z] \\ = 0, \end{aligned} \quad (33)$$

$$\begin{aligned} i\Delta\omega \delta B_\phi + \left[\frac{\partial v_\phi}{\partial r} - \frac{v_\phi}{r} \right] \delta B_r - B_\phi \frac{\partial \delta v_r}{\partial r} \\ + [\eta_O + \eta_A] \left[\frac{\partial^2 \delta B_\phi}{\partial r^2} + \frac{1}{r} \frac{\partial \delta B_\phi}{\partial r} - k_\phi^2 \delta B_\phi - \frac{\delta B_\phi}{r^2} + \frac{2}{r} ik_\phi \delta B_r \right] \\ + \eta_H \left[ik_\phi \left(\frac{\partial \delta B_z}{\partial r} - \frac{\delta B_z}{r} \right) \right] \\ = 0, \end{aligned} \quad (34)$$

$$\begin{aligned} i\Delta\omega \delta B_z + ik_\phi B_\phi \delta v_z \\ + \eta_O \left[\frac{\partial^2 \delta B_z}{\partial r^2} + \frac{1}{r} \frac{\partial \delta B_z}{\partial r} - k_\phi^2 \delta B_z \right] \\ + \eta_A \left[-k_\phi^2 \delta B_z \right] \\ + \eta_H \left[ik_\phi \left(-\frac{\partial \delta B_\phi}{\partial r} - \frac{\delta B_\phi}{r} + ik_\phi \delta B_r \right) \right] \\ = 0. \end{aligned} \quad (35)$$

In the limit of pure B_ϕ and $k_z = 0$, all three non-ideal MHD effects are present. Ohmic resistivity and ambipolar diffusion exhibit identical terms in both radial and azimuthal components of the induction equation. We set $\delta B_z = \delta v_z = 0$ because δB_z and δv_z solely appear in eqs (32) and (35).

2.3.3 non-ideal MHD limit: pure B_z

For a pure B_z field, the vertical component of the momentum equation yields $\delta v_z = 0$, while the remaining two linearized momentum equations are

$$i\Delta\omega \delta v_r + 2\Omega \delta v_\phi - \frac{\partial \delta \Psi}{\partial r} - \frac{1}{4\pi\rho} \left[B_z \frac{\delta B_z}{\partial r} \right] = 0, \quad (36)$$

$$i\Delta\omega \delta v_\phi - \frac{\kappa^2}{2\Omega} \delta v_r - ik_\phi \delta \Psi + \frac{1}{4\pi\rho} \left[-ik_\phi B_z \delta B_z \right] = 0. \quad (37)$$

The non-ideal MHD effects manifest in the induction equation (4),

$$\begin{aligned} i\Delta\omega \delta B_r + \eta_O \left[\frac{\partial^2 \delta B_r}{\partial r^2} + \frac{1}{r} \frac{\partial \delta B_r}{\partial r} - k_\phi^2 \delta B_r - \frac{\delta B_r}{r^2} - \frac{2}{r} ik_\phi \delta B_\phi \right] \\ = 0, \end{aligned} \quad (38)$$

$$\begin{aligned}
& i\Delta\omega\delta B_\phi + \left[\frac{\partial v_\phi}{\partial r} - \frac{v_\phi}{r} \right] \delta B_r \\
& + \eta_0 \left[\frac{\partial^2 \delta B_\phi}{\partial r^2} + \frac{1}{r} \frac{\partial \delta B_\phi}{\partial r} - k_\phi^2 \delta B_\phi - \frac{\delta B_\phi}{r^2} + \frac{2}{r} i k_\phi \delta B_r \right] \\
& = 0, \tag{39}
\end{aligned}$$

$$\begin{aligned}
& i\Delta\omega\delta B_z + B_z \left[\frac{1}{L_\rho} \delta v_r - \frac{i\Delta\omega}{c_s^2} \delta \Psi \right] \\
& + [\eta_0 + \eta_A] \left[\frac{\partial^2 \delta B_z}{\partial r^2} + \frac{1}{r} \frac{\partial \delta B_z}{\partial r} - k_\phi^2 \delta B_z \right] \\
& = 0. \tag{40}
\end{aligned}$$

In the limit of pure B_z and $k_z = 0$, only Ohmic resistivity and ambipolar diffusion contribute to the linearized induction equations, but not Hall drift. Ambipolar diffusion manifests only in the vertical component of the induction equation, exhibiting identical terms to Ohmic resistivity. Furthermore, δB_r and δB_ϕ are involved only in eqs (38) and (39), and hence can be set as $\delta B_r = \delta B_\phi = 0$.

3 NUMERICAL METHODS

We solve the linearized equations presented in §2.3 numerically. Two numerical methods are employed to solve ODE eigenvalue value problems: the pseudospectral method (§3.1) and the finite difference method (§3.2).

We find that the spectral method, via the Python package DEDALUS, outperforms the finite difference method. The finite difference method produced a number of spurious modes with oscillation frequencies ω_r that closely resembled those of RWI modes, particularly when incorporating Hall drift. Consequently, we use the spectral method as the primary numerical approach for solving the ODE systems and compare its results to those obtained from the finite difference method for a selected range of parameters. The details of these two methods are provided below.

3.1 Pseudospectral method

Pseudospectral methods, also known as orthogonal collocation methods, approximate the solution of differential equations at selected collocation points, by a weighted sum of orthogonal basis functions, which are often chosen to be orthogonal polynomials up to a certain degree. Chebyshev polynomials of the first kind T_n , where $n = 0, 1, 2, \dots, N-1$, are chosen in our problem, for which the eigenfunctions are expanded in. The radial domain, that spans $r \in [0.4, 1.6]$, is discretized into N Chebyshev collocation points. To minimize the interpolation error, these nodes are non-uniform and are selected as the roots of N th degree Chebyshev polynomial T_N , which cluster near the ends of the domain (Figure 1; Burns et al. 2020).

The differential equations described in §2 construct standard linear eigenvalue problems. Written compactly in a generalized matrix form, it is

$$A\vec{x} = \mathcal{L}\vec{x} + \omega\mathcal{M}\vec{x} = 0, \tag{41}$$

where ω is the eigenvalue, $\vec{x} = [\delta\vec{v}_r, \delta\vec{B}_r, \delta\vec{\rho}, \dots]^T$ is a vector of eigenfunctions with M perturbed quantities, and $A, \mathcal{L}, \mathcal{M}$ are

$MN \times MN$ sized matrices, with \mathcal{L} composed of linear operators. We employ DEDALUS¹, a general purpose spectral code for differential equations (Burns et al. 2020), to solve the linear eigenvalue problem described above. We utilize the dense solver method by `solve_dense` in DEDALUS, for which matrix A is converted to dense arrays, and the `scipy.linalg.eig` routine in Python is utilized to directly solve the eigenvalue problem.

Generally, a numerical resolution of $N = 256$ is adopted. Spurious solutions can arise due to the truncation of differential equations to finite-dimensional algebraic equations (Zebib 1987; McFadden et al. 1990). Most spurious modes are eliminated by increasing the numerical resolution by 1.5 times. By comparing solutions between low and high resolutions, we retain only the valid modes within a tolerance of 10^{-6} .

3.2 Finite difference method

In finite difference method, we approximate the ODEs by finite difference equations, a technique previously adopted in RWI literature by Ono et al. (2016); Liu & Bai (2023). We discretize the ODEs on a grid with $N = 1001$ points and uniform spacing h , spanning the domain $r \in [0.4, 1.6]$. The system can be compactly expressed using matrices. The $MN \times MN$ sized matrix A , corresponding to the set of ODEs, is written as

$$A\vec{x} = \begin{vmatrix} A_{00} & \dots & A_{0,M-1} \\ \dots & \dots & \dots \\ A_{M-1,0} & \dots & A_{M-1,M-1} \end{vmatrix} \vec{x} = 0. \tag{42}$$

Matrix A consists of $M \times M$ submatrices A_{ij} , for $i, j = 0, \dots, M-1$. The value of M is set by the number of perturbed quantities contained in the system of ODEs. Each submatrix A_{ij} has a size of $N \times N$. The vector of perturbed quantities is expressed as $\vec{x} = [\delta\vec{v}_r, \delta\vec{B}_r, \delta\vec{\rho}, \dots]^T$, where each perturbed quantity, for example, $\delta\vec{v}_r = \delta\vec{v}_r(r_k)$, is evaluated at grid points r_k , for $k = 0, \dots, N-1$.

The entries of A_{ij} are filled in by constructing the linear operators of the first derivative d/dr and the second derivative d^2/dr^2 . We adopt the central differencing scheme to obtain the linear operators of the first derivative (Liu & Bai 2023),

$$A_{ij,n,n-1} = -\frac{1}{2h}, \tag{43}$$

$$A_{ij,n,n+1} = \frac{1}{2h}, \tag{44}$$

and the second derivative,

$$A_{ij,n,n-1} = \frac{1}{h^2}, \tag{45}$$

$$A_{ij,n,n} = -\frac{2}{h^2}, \tag{46}$$

$$A_{ij,n,n+1} = \frac{1}{h^2}, \tag{47}$$

for $n = 1, \dots, N-2$.

¹ <https://dedalus-project.org/>

The differential equations described in §2 form standard linear eigenvalue problems. The eigenvalue (ω) and the corresponding eigenfunction (perturbed quantities \vec{x}) are readily determined by utilizing `numpy.linalg.eig` routine in Python.

3.3 Boundary conditions

To accommodate the density waves, WKB boundary conditions are imposed, and the linear operator $d/dr - ik_r = 0$ is applied to the boundary.

In the finite difference method, the boundary conditions involve in the zeroth and $(N - 1)$ th row of A_{ij} . Using the forward differencing scheme for the outer boundary conditions and the backward differencing scheme for the inner boundary conditions, the entries of A_{ij} at boundaries can be written as

$$A_{ij,00} = -\frac{1}{h}, \quad (48)$$

$$A_{ij,01} = \frac{1}{h} - ik_r, \quad (49)$$

$$A_{ij,N-1,N-2} = -\frac{1}{h} - ik_r, \quad (50)$$

$$A_{ij,N-1,N-2} = \frac{1}{h}. \quad (51)$$

To solve for k_r at the boundaries, away from the RWI region where the background quantities vary slowly over radius, we use WKB analysis by assuming $\delta v, \delta B, \delta \rho \dots \propto \exp(ik_r r)$. Substituting the derivatives by k_r , we obtain $B(k_r, \omega) \vec{y} = 0$ at the boundaries, where B is a matrix containing k_r and ω , and $\vec{y} = [\delta v_r, \delta B_r, \delta \rho, \dots]^T$. Both B and \vec{y} are evaluated at r_0 and r_{N-1} . We take ω to be the value obtained from last β . This approach works if we gradually decrease β values in the domain of interest. Now the only unknown in matrix B is k_r , which is determined using the Newton-Raphson method by setting the determinant of B to zero, $\det B(k_r) = 0$. The implementation of this method utilizes the source code of `scipy.optimize.newton` as a reference. The iteration converges within five steps for a tolerance of 10^{-10} .

We choose azimuthal mode number $m = 2, 3, 4, 5$ for the calculations presented in this work. For smaller or larger mode numbers, the growth rates can be relatively small and are sensitive to the grid resolution. We note that when $m = 1$, the inner boundary condition differs from the WKB one described earlier. In the hydrodynamic limit, the inner boundary lies within the evanescent region, and the inner Lindblad resonance is absent. Instead, one can assume a power-law behavior in r and ensure regularity at $r = 0$ (Ono et al. 2016).

4 RESULTS

The numerical solutions are presented for the ideal MHD limit (§4.1), Ohmic resistivity (§4.2), ambipolar diffusion (§4.3), and the Hall drift (§4.4), respectively. The analysis will be focused on the RWI growth rates, as the eigenfunctions are similar to those in the pure hydrodynamic limit; two Rossby waves are located on each side of the corotation radius, with density waves excited at the inner and outer

Lindblad resonances, propagating away from the corotation radius (e.g., Lovelace & Romanova 2014). Note that in the Figures shown below, we select and present only the fastest growing mode for a specific parameter, though a handful of slower growing modes also exist.

4.1 Ideal MHD

To analyze the numerical solutions in the ideal MHD limit, we begin with the pure B_ϕ field. The top panel of Figure 1 depicts normalized RWI growth rates γ/Ω_{K0} as a function of plasma β , for different azimuthal mode numbers $m = 2, 3, 4, 5$ at an infinite vertical wavelength, $k_z = 0$. At $\beta = 100$, the growth rates nearly recover the hydrodynamic RWI results, with the maximum growth rate observed at $m = 4$ for the chosen set of parameters. As β exceeds 100, the curves begin to plateau. Conversely, as plasma β decreases, the growth rates diminish for all azimuthal mode numbers m investigated. This suggests that increased magnetization suppresses RWI growth. It can be interpreted as that the magnetic fields are perfectly coupled with gas in the ideal MHD limit, potentially hindering the free movement of perturbed gas. The top panel of Figure 2 shows growth rates for different vertical wavenumbers $k_z = 0, 1/10H, 1/5H$ at $m = 4$. It is evident that increasing vertical wavenumbers tend to reduce RWI growth rates across the range of β values explored.

Figure 3 displays the RWI growth rates in the ideal MHD limit for the pure B_z field. Unlike in the pure B_ϕ field, where growth rates monotonically decrease towards smaller β , different azimuthal mode numbers m exhibit distinct behaviors across the range of β (top panel). The parameter space of β is now extended down to 0.01, in order to provide ample coverage to observe the trend in growth rates. For relatively large $m = 5$, the RWI growth rates decrease monotonically as β decreases, similar to pure B_ϕ model. Conversely, smaller $m = 2, 3, 4$ show an increase in growth rates as β decreases, followed by a decline as β drops further. The peak of the growth rates occurs at higher β values for larger m . This is in agreement with Yu & Lai (2013), who observed a peak in growth rate for $m = 4$ around $\beta \approx 0.1$, as shown in their Figure 2. As β approaches 0.01, the growth rates asymptotically approach a stable value for each m investigated. When there is a finite vertical wavelength ($k_z \neq 0$), the growth rates diminish with higher k_z depicted in the top panel of Figure 4.

4.2 Ohmic resistivity

Next, we examine Ohmic resistive disks. The middle panel of Figure 1 shows RWI growth rates as a function of the Ohmic Elsässer number Λ at $\beta = 2$. As $\Lambda \rightarrow \infty$, the growth rates tend to approach those of ideal MHD limit. For example, at $\beta \approx 2.212$ the growth rates calculated for $m = 2, 3, 4, 5$ in the ideal MHD limit are $\omega/\Omega_{K0} \approx 1.974 + 0.0554i, 2.963 + 0.0708i, 3.956 + 0.0726i, 4.949 + 0.0647i$, respectively (top panel; Figure 1). Correspondingly, the growth rates calculated for resistive disks at $\Lambda = 100$ are $\omega/\Omega_{K0} \approx 1.973 + 0.0528i, 2.963 + 0.0666i, 3.956 + 0.0666i, 4.949 + 0.0526i$. As Ohmic Elsässer number decreases, the growth rates for all m models gradually increase. At $\Lambda = 10^{-2}$, they converge towards hydrodynamic results. For instance, at $\beta =$

100, the growth rates for $m = 2, 3, 4, 5$ in the ideal MHD limit are $\omega/\Omega_{K0} \approx 1.976 + 0.0892i, 2.966 + 0.118i, 3.957 + 0.131i, 4.950 + 0.127i$, respectively (top panel; Figure 1). The corresponding growth rates computed for the resistive disks at $\Lambda = 0.01$ are $\omega/\Omega_{K0} \approx 1.971 + 0.0881i, 2.960 + 0.103i, 3.948 + 0.130i, 4.938 + 0.130i$, respectively.

The pure B_z disk follows the similar trend as the pure B_ϕ disk. As Λ approaches infinity, the growth rates resemble those in the ideal MHD limit. Specifically, the growth rates at $\beta \approx 2.212$ in the ideal MHD limit are $\omega/\Omega_{K0} \approx 1.973 + 0.0979i, 2.963 + 0.126i, 3.956 + 0.136i, 4.949 + 0.128i$, respectively (top panel; Figure 3). For comparison, at $\beta = 2$ and $\Lambda = 100$, the RWI growth for $m = 2, 3, 4, 5$ are, respectively, $\omega/\Omega_{K0} \approx 1.973 + 0.0984i, 2.963 + 0.126i, 3.956 + 0.136i, 4.948 + 0.128i$. As the Ohmic Elsässer number decreases, growth rates of different m models all converge towards hydrodynamic results. This can be readily seen by that at $\beta = 100$, the growth rates for $m = 2, 3, 4, 5$ in the ideal MHD limit are $\omega/\Omega_{K0} \approx 1.976 + 0.0903i, 2.966 + 0.120i, 3.958 + 0.133i, 4.950 + 0.129i$, respectively (top panel; Figure 3). The corresponding growth rates in the resistive disks at $\Lambda = 0.01$ and $\beta = 2$ are $\omega/\Omega_{K0} \approx 1.977 + 0.0878i, 2.960 + 0.118i, 3.963 + 0.122i, 4.928 + 0.139i$, respectively. Among the explored azimuthal mode numbers, only the $m = 2$ curve rises with Λ , while the others drop. This is due to the peak pattern observed for $m = 3, 4, 5$ in the ideal MHD limit (top panel; Figure 3).

The middle panels of Figure 2 and Figure 4 show variations in growth rates with Ohmic Elsässer number Λ at $m = 4$ for different vertical wavenumbers k_z . It is evident that the growth rates decrease steadily with the vertical wavenumber k_z .

4.3 ambipolar diffusion

Ambipolar diffusion shares the exact perturbation equations to Ohmic resistivity if $k_z = 0$ (§2.3). Consequently, results obtained for resistivity can directly apply to it. The curves obtained for Am overlap exactly with those obtained for Λ in the middle panels of Figure 1 and Figure 3.

Nevertheless, for non-zero k_z the induction equations differ between resistivity and ambipolar diffusion. In the pure B_ϕ model, the ϕ -component of the induction equation shares the same terms for resistivity and ambipolar diffusion, while the other two components differ. Despite these differences, the growth rates in the ambipolar diffusion limit closely approximate those in the resistivity limit when $k_z = 1/10H, 1/5H$ (middle panel; Figure 2). In the pure B_z model, we suspect the modes obtained are spurious and provide a detailed explanation in Appendix B.

4.4 The Hall drift

Unlike resistivity or ambipolar diffusion, Hall physics is sensitive to rotation/radial shear (Latter & Kunz 2022). This is evident by reversing the sign of B in the induction equation. In the limit of an axial field and wavenumber, the Hall Elsässer number is written by $\text{Ha} = v_{Az}^2/v_H^2$, where $v_H^2 \equiv \Omega B_z c / (2\pi e n_e)$ is the square of the Hall velocity. It follows that v_H^2 , though squared, and Ha take negative (positive) values if $\boldsymbol{\Omega}$ and \mathbf{B}_z are oriented oppositely (parallel). With more general field geometries and wavenumbers, the

sign of Ha depends on $(\boldsymbol{\Omega} \cdot \mathbf{k})(\mathbf{B} \cdot \mathbf{k})$ (Balbus & Terquem 2001). For a fixed direction of rotation, the toroidal field reverses its sign along with vertical field. We explore positive and negative Ha in pure B_ϕ and B_z disk models.

In the case of pure B_ϕ and $k_z = 0$, the Hall drift has a similar influence as resistivity and ambipolar diffusion (bottom panel; Figure 1). Moreover, the results obtained for Ha and $-\text{Ha}$ overlap. As $\text{Ha}/- \text{Ha} \rightarrow \infty$, the growth rate resembles those of ideal MHD, while as $\text{Ha}/- \text{Ha} \rightarrow 0$, the growth rates revive and approach hydrodynamic results. For example, at $\beta \approx 2$ for $m = 2, 3, 4, 5$ the growth rates in the ideal MHD limit are provided in §4.2. In the Hall drift limit at $\text{Ha} = 100$, the corresponding growth rates are $\omega/\Omega_{K0} \approx 1.973 + 0.0526i, 2.963 + 0.0675i, 3.956 + 0.0683i, 4.949 + 0.0560i$, respectively. At $\beta = 100$ and $m = 2, 3, 4, 5$, the ideal MHD growth rates are also given in §4.2. In the Hall drift limit at $\text{Ha} = 0.01$ and $\beta = 2$, the corresponding growth rates are $\omega/\Omega_{K0} \approx 1.971 + 0.0896i, 2.960 + 0.121i, 3.950 + 0.135i, 4.949 + 0.133i$, respectively. The bottom panel of Figure 2 shows growth rates at $k_z \neq 0$. The variation of vertical wavelengths does not significantly influence the RWI growth. The sign of Ha does not yield distinct values of γ when $k_z \neq 0$ either.

In the case of pure B_z , the Hall terms only appear in the induction equations when the wavelength is finite ($k_z \neq 0$). As shown in bottom panel of Figure 4, when vertical wavenumber is very small, for example $k_z = 1/50H$, the growth rates do not vary much across $\text{Ha}/- \text{Ha}$, as Hall terms vanish at $k_z = 0$. Increasing k_z generically diminish the RWI growth. Furthermore, positive and negative Ha exhibit distinct behaviors; positive Ha results in a trough at $\text{Ha} \approx 0.1$, whereas negative Ha results in a peak at around the same location, slightly shifted towards larger $|\text{Ha}|$.

5 SUMMARY

We studied the magnetized and lightly ionized RWI by Eulerian perturbations. The framework is three-dimensional and radially global. Ideal MHD and non-ideal MHD effects, including Ohmic resistivity, ambipolar diffusion, and the Hall drift are considered. Taking advantage of the barotropic fluid assumption, the perturbation equations form standard eigenvalue problems. The spectral method via DEDALUS excels in resolving the eigenmodes. Our results are summarized as follows.

For a pure B_ϕ field:

- When gas and magnetic fields are perfectly coupled, RWI growth rates increase with β . Strong magnetization tends to impede RWI. For all three non-ideal MHD effects, as Elsässer numbers approach infinity, the results resemble the ideal MHD limit; as Elsässer numbers approach zero, the results resemble the hydrodynamic limit. In the limits of ideal MHD, Ohmic resistivity, and ambipolar diffusion, non-zero vertical wavenumbers generically diminish RWI growth compared to $k_z = 0$ limit. In Hall-dominated disks, non-zero wavenumbers do not significantly impact the results. The sign of Ha does not yield different results.

For a pure B_z field:

- In the ideal MHD limit, RWI growth rates can either increase or decrease with β , depending on the azimuthal mode number m . In the limit of resistivity, similar to the B_ϕ model,

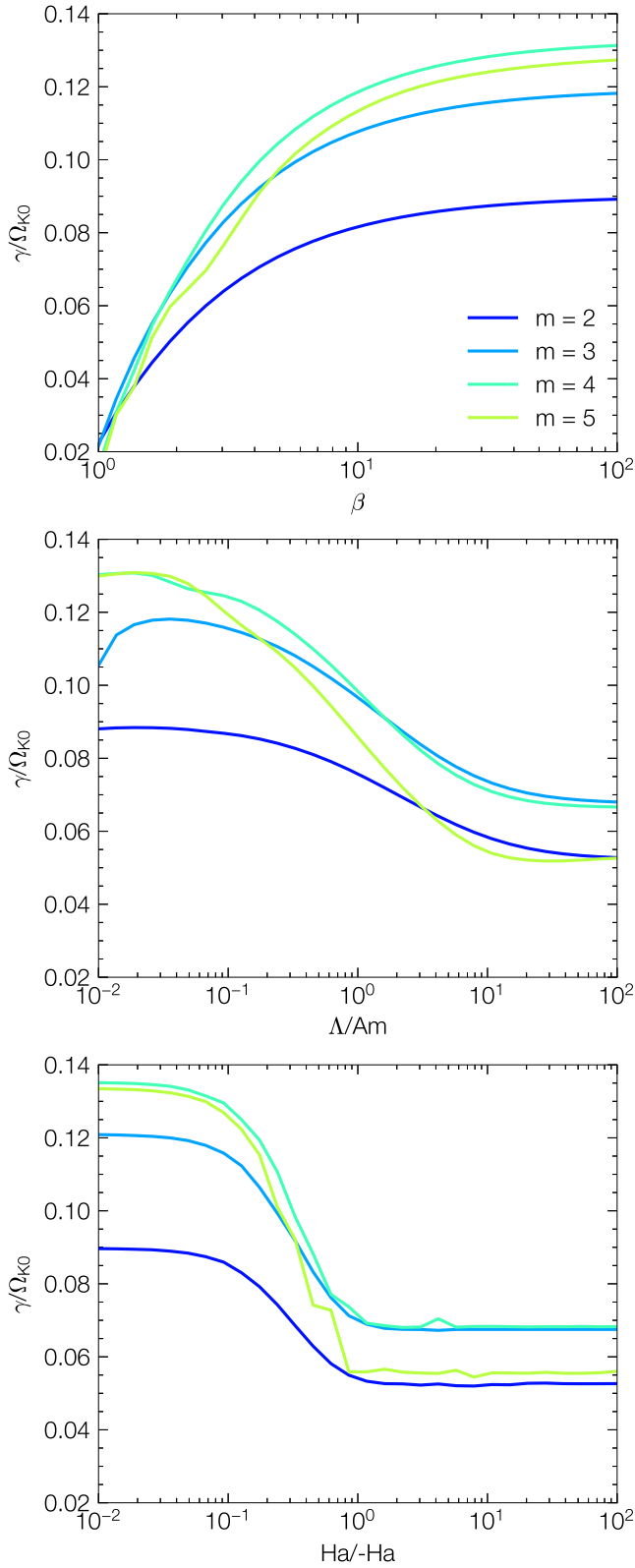


Figure 1. Pure B_ϕ and $k_z = 0$. Top panel: normalized RWI growth rates γ/Ω_{K0} vs plasma β in the ideal MHD limit for different m . Middle panel: growth rates vs Ohmic (Λ) or ambipolar (Am) Elsässer numbers at $\beta = 2$. Bottom panel: growth rates vs Hall Elsässer number Ha or $-Ha$ at $\beta = 2$.

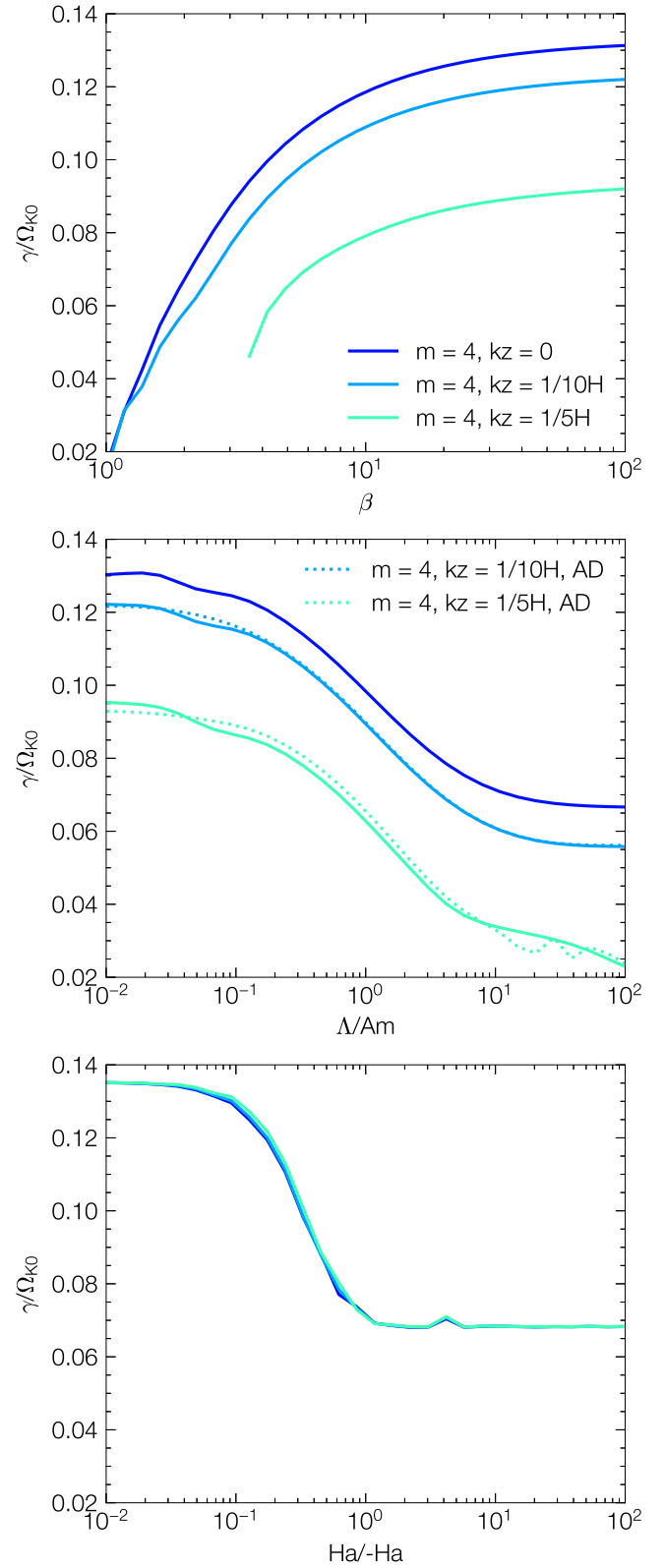


Figure 2. Pure B_ϕ and $k_z \neq 0$. Top panel: normalized RWI growth rates γ/Ω_{K0} vs β in the ideal MHD limit for different $k_z = 0, 1/10H, 1/5H$ at fixed $m = 4$. Middle panel: growth rates vs Ohmic (Λ ; solid) or ambipolar (Am ; dotted) Elsässer numbers at $\beta = 2$. Bottom panel: growth rates vs Hall Elsässer number Ha or $-Ha$ at $\beta = 2$.

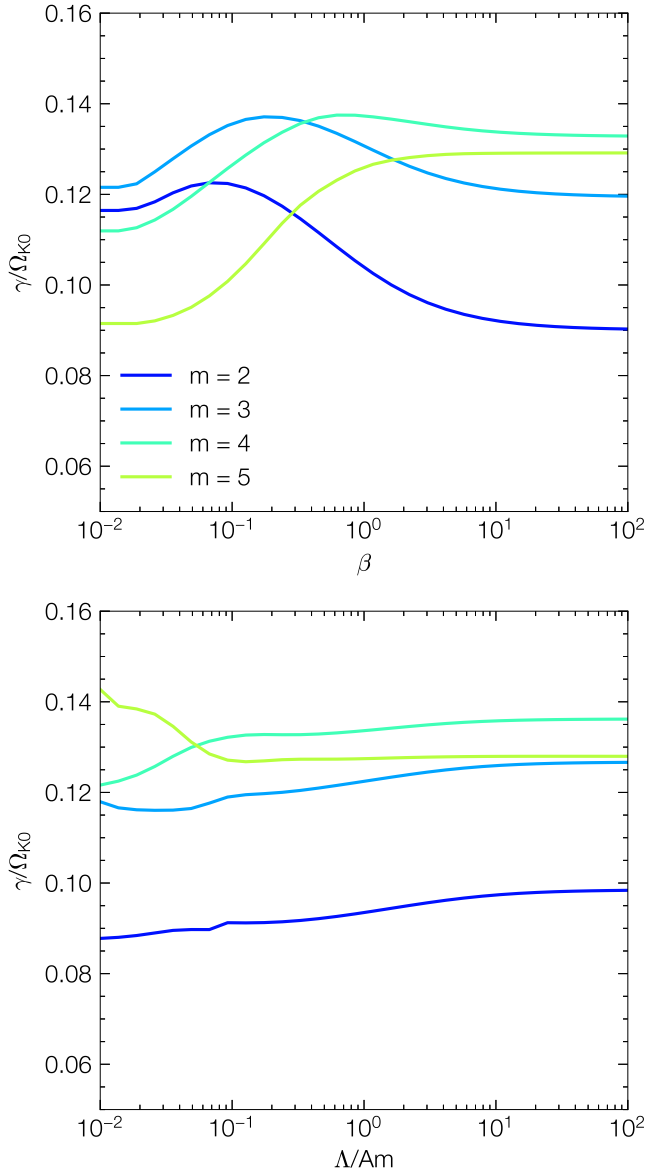


Figure 3. Same as top and middle panels of Figure 1, but for pure B_z disks.

as Elsässer numbers approach infinity, the results resemble the ideal MHD limit. As Elsässer numbers approach zero, the results resemble the hydrodynamic limit. In the limit of ideal MHD and resistivity, similar to the B_ϕ model, vertical wavenumbers generically diminish RWI growth. Hall drift only appears when $k_z \neq 0$. The sign of Ha slightly complicates the growth rates.

6 DISCUSSION

We compare the linear growth rates between RWI and MRI. We follow the framework, derivations, and analyses described in [Latter & Kunz \(2022\)](#) for MRI. In most cases of it, we consider channel modes with $k_x/k_z = 0$, a pure vertical field B_z

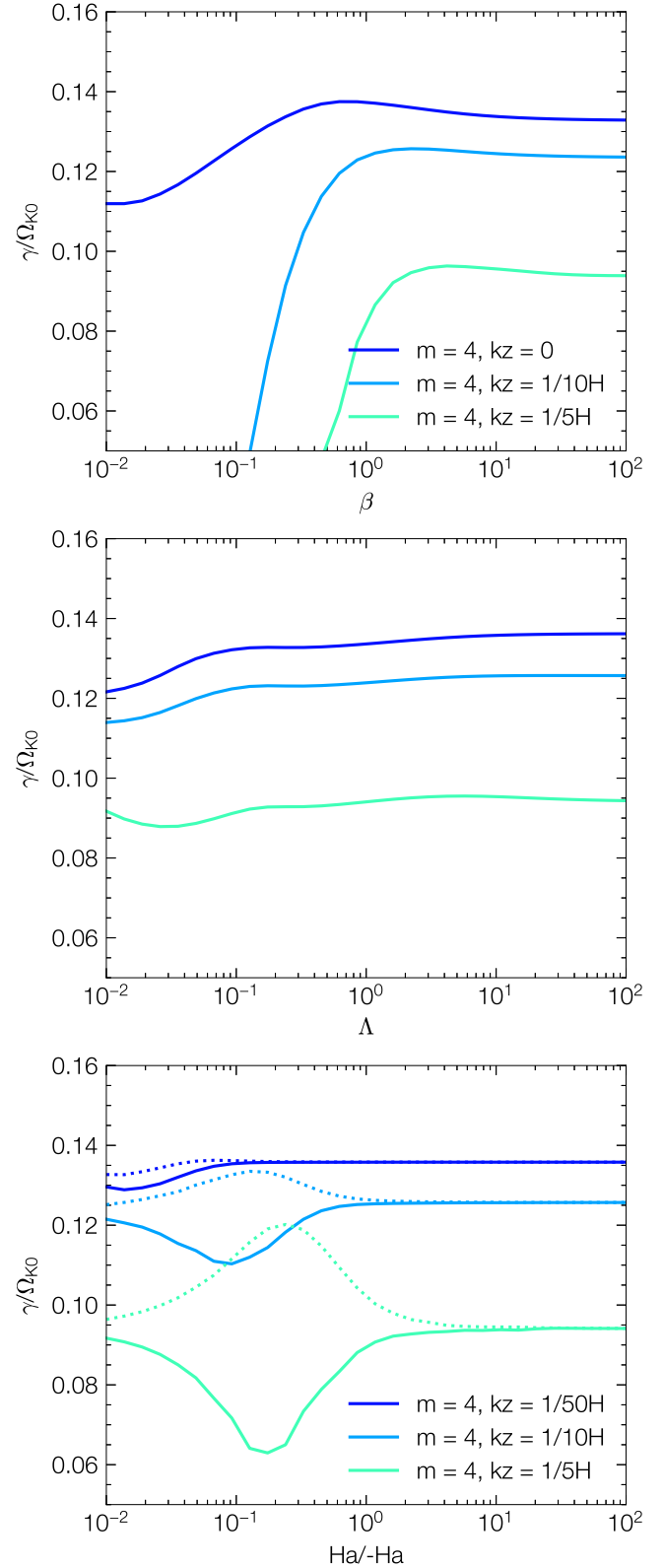


Figure 4. Same as Figure 2, but for pure B_z disks. The middle panel only shows growth rates vs Ohmic Elsässer numbers (Λ). The bottom panel shows positive (solid) and negative (dotted) Ha at $k_z = 1/50H, 1/10H, 1/5H$, respectively.

and β_z , Keplerian rotation, and no vertical shear. We also consider azimuthal fields in the ambipolar diffusion dominated regime.

We start with the simplest ideal MHD limit. Eq (29) in [Latter & Kunz \(2022\)](#) shows the bi-quadratic dispersion relation, and the MRI growth rate s is found to be:

$$\frac{2s^2}{\Omega^2} = -\left(\frac{2k_z^2 v_{Az}^2}{\Omega^2} + 1\right) + \left(\frac{16k_z^2 v_{Az}^2}{\Omega^2} + 1\right)^{1/2}, \quad (52)$$

where $v_{Az} = B_z/\sqrt{4\pi\rho}$ is the vertical Alfvén velocity. The maximum growth rate $s = 3/4\Omega$ occurs when $k_z^2 v_{Az}^2 = 15/16\Omega^2$ as expected. On the other hand, growth rates vanish when $k_z^2 v_{Az}^2 = 3\Omega^2$. In a realist protoplanetary disk, the vertical wavelength should be shorter than the pressure scale height, or $k_z > 1/H$. Therefore, the criteria for the existence of MRI modes is $\beta_z > q_R^{-1}$, where $q_R = -\partial \ln \Omega / \partial \ln R$ is the dimensionless orbital shear, and has $q_R = 3/2 \sim O(1)$ for Keplerian rotation. The maximum growth can occur when $\beta_z > 32/15$. Both criteria can be readily satisfied in protoplanetary disks, allowing linear MRI modes to easily surpass RWI modes.

For resistivity dominated disks, the instability criterion for MRI channel modes is presented in eq (34) of [Latter & Kunz \(2022\)](#). Requiring the vertical wavelengths to be longer than the thickness of the disk yields

$$\beta_z > q_R^{-1}(1 + \Lambda^{-2}). \quad (53)$$

If $\Lambda \rightarrow \infty$, the system is almost in the ideal MHD regime, and $\beta_z > q_R^{-1}$ is required for channel modes to emerge. Thus, MRI surpasses RWI as shown above. If $\Lambda \ll 1$, the system is strongly resistivity dominated, and $\beta_z \gtrsim \Lambda^{-2}$. In this regime, RWI modes resemble hydrodynamic results, and can surpass MRI. For a zero B_ϕ field, the instability criteria and physical behavior of ambipolar diffusion is very similar to the Ohmic regime.

For a non-zero B_ϕ field, the MRI channel modes are diminished by small Am , for which regime ambipolar diffusion shear instability (ADSI) can emerge ([Desch 2004](#); [Kunz & Balbus 2004](#); [Kunz 2008](#)). We start with the rather simple pure MRI channel modes. These modes exist when

$$\beta_z > q_R^{-1}(1 + Am^{-2}B^2/B_z^2). \quad (54)$$

The presence of azimuthal fields contributes to stabilizing the MRI. In three-dimensional global numerical simulations incorporating ambipolar diffusion, a typical ratio of $B_\phi/B_z \sim O(10)$ has been observed ([Cui & Bai 2022](#)). Using this ratio, channel modes occur under conditions where $\beta_z \gtrsim 10^4, 10^2, 1$ for $Am = 0.1, 1, 10$, respectively. Thereby, RWI may dominate over MRI for $Am \lesssim 0.1$ in a protoplanetary disk. On the other hand, ADSI becomes significant when channel modes are diminished. ADSI modes have $|k_x/k_z| > 0$. Although these modes can always emerge for sufficiently large $|k_x/k_z|$, their growth rates might be rather small ([Latter & Kunz 2022](#)). To investigate the dominance between MRI/ADSI and RWI, we compute the growth rates by the ambipolar dispersion relation shown in eq (31) of [Kunz & Balbus \(2004\)](#). We utilize $B_\phi/B_z \sim O(10)$ and set a critical growth rate threshold at $0.01\Omega_K$ (see middle panels of [Figure 1](#) and [Figure 3](#)). Under these conditions, no modes satisfy the growth rate criterion for $Am < 1$, leading us to conclude that RWI surpasses MRI/ADSI in this regime.

Lastly, we examine the Hall dominated regime. Positive Ha

exhibits fast growth rates around $\sim O(0.75\Omega_K)$, stemming from a blend of MRI and Hall shear instability. There are three regimes associate with negative Ha. For $Ha < -0.25$, we are in the Hall modified and diffusive MRI regimes, for which growth rates are rather fast $\sim O(0.75\Omega_K)$. For $Ha > -0.25$, there is no instability possible, rendering it ideal for RWI modes to grow.

ACKNOWLEDGEMENTS

CC acknowledges funding from Natural Sciences and Engineering Research Council of Canada and UK STFC grant ST/T00049X/1. AT acknowledges summer studentship from the Centre for Mathematical Sciences, University of Cambridge. CY is supported by the National SKA Program of China (grant 2022SKA0120101) and the National Natural Science Foundation of China (grants 11873103 and 12373071). MKL is supported by the National Science and Technology Council (grants 112-2112-M-001-064-, 113-2124-M-002-003-) and an Academia Sinica Career Development Award (AS-CDA-110-M06).

DATA AVAILABILITY

The data underlying this article will be shared on reasonable request to the corresponding author.

REFERENCES

- Armitage P. J., 2011, [ARA&A](#), **49**, 195
 Bai X.-N., 2011, [ApJ](#), **739**, 51
 Balbus S. A., Hawley J. F., 1991, [ApJ](#), **376**, 214
 Balbus S. A., Terquem C., 2001, [ApJ](#), **552**, 235
 Béthune W., Latter H., 2020, [MNRAS](#), **494**, 6103
 Blaes O. M., Balbus S. A., 1994, [ApJ](#), **421**, 163
 Burns K. J., Vasil G. M., Oishi J. S., Leconte D., Brown B. P., 2020, [Physical Review Research](#), **2**, 023068
 Cimerman N. P., Rafikov R. R., 2023, [MNRAS](#), **519**, 208
 Cui C., Bai X.-N., 2020, [ApJ](#), **891**, 30
 Cui C., Bai X.-N., 2021, [MNRAS](#), **507**, 1106
 Cui C., Bai X.-N., 2022, [MNRAS](#), **516**, 4660
 Cui C., Lin M.-K., 2021, [MNRAS](#), **505**, 2983
 Desch S. J., 2004, [ApJ](#), **608**, 509
 Flock M., Fromang S., Turner N. J., Benisty M., 2017, [ApJ](#), **835**, 230
 Fuente A., et al., 2017, [ApJ](#), **846**, L3
 Fung J., Ono T., 2021, [ApJ](#), **922**, 13
 Galli D., Shu F. H., 1993, [ApJ](#), **417**, 220
 Girart J. M., Rao R., Marrone D. P., 2006, [Science](#), **313**, 812
 Girart J. M., Beltrán M. T., Zhang Q., Rao R., Estalella R., 2009, [Science](#), **324**, 1408
 Godon P., Livio M., 1999, [ApJ](#), **523**, 350
 Goldreich P., Schubert G., 1967, [ApJ](#), **150**, 571
 Goldreich P., Ward W. R., 1973, [ApJ](#), **183**, 1051
 Güttler C., Blum J., Zsom A., Ormel C. W., Dullemond C. P., 2010, [A&A](#), **513**, A56
 Hammer M., Kratter K. M., Lin M.-K., 2017, [MNRAS](#), **466**, 3533
 Huang P., Isella A., Li H., Li S., Ji J., 2018, [ApJ](#), **867**, 3
 Kunz M. W., 2008, [MNRAS](#), **385**, 1494
 Kunz M. W., Balbus S. A., 2004, [MNRAS](#), **348**, 355
 Latter H. N., Kunz M. W., 2022, [MNRAS](#), **511**, 1182
 Latter H. N., Papaloizou J., 2018, [MNRAS](#), **474**, 3110
 Lesur G., 2021, [Journal of Plasma Physics](#), **87**, 205870101

- Lesur G., Papaloizou J. C. B., 2009, *A&A*, **498**, 1
- Li H., Finn J. M., Lovelace R. V. E., Colgate S. A., 2000, *ApJ*, **533**, 1023
- Li H., Colgate S. A., Wendroff B., Liska R., 2001, *ApJ*, **551**, 874
- Li Y.-P., Li H., Li S., Birnstiel T., Drazkowska J., Stammler S., 2020, *ApJ*, **892**, L19
- Lin M.-K., 2012, *MNRAS*, **426**, 3211
- Lin M.-K., Hsu C.-Y., 2022, *ApJ*, **926**, 14
- Lin M.-K., Papaloizou J. C. B., 2011, *MNRAS*, **415**, 1426
- Lin C. C., Shu F. H., 1964, *ApJ*, **140**, 646
- Liu H., Bai X.-N., 2023, *MNRAS*, **526**, 80
- Lovelace R. V. E., Romanova M. M., 2014, *Fluid Dynamics Research*, **46**, 041401
- Lovelace R. V. E., Li H., Colgate S. A., Nelson A. F., 1999, *ApJ*, **513**, 805
- Lyra W., Mac Low M.-M., 2012, *ApJ*, **756**, 62
- McFadden G., Murray B., Boisvert R., 1990, *Journal of Computational Physics*, **91**, 228
- Meheut H., Keppens R., Casse F., Benz W., 2012, *A&A*, **542**, A9
- Miranda R., Lai D., Méheut H., 2016, *MNRAS*, **457**, 1944
- Miranda R., Li H., Li S., Jin S., 2017, *ApJ*, **835**, 118
- Muto T., et al., 2015, *PASJ*, **67**, 122
- Nelson R. P., Gressel O., Umurhan O. M., 2013, *MNRAS*, **435**, 2610
- Ono T., Muto T., Takeuchi T., Nomura H., 2016, *ApJ*, **823**, 84
- Pandey B. P., Wardle M., 2012, *MNRAS*, **423**, 222
- Riols A., Lesur G., 2019, *A&A*, **625**, A108
- Rometsch T., Ziampras A., Kley W., Béthune W., 2021, *A&A*, **656**, A130
- Surville C., Mayer L., 2019, *ApJ*, **883**, 176
- Surville C., Mayer L., Lin D. N. C., 2016, *ApJ*, **831**, 82
- Tsang D., Lai D., 2008, *MNRAS*, **387**, 446
- Wang L., Bai X.-N., Goodman J., 2019, *ApJ*, **874**, 90
- Wardle M., 1999, *MNRAS*, **307**, 849
- Wardle M., 2007, *Ap&SS*, **311**, 35
- Weidenschilling S. J., 1977, *Ap&SS*, **51**, 153
- Weiss B. P., Bai X.-N., Fu R. R., 2021, *Science Advances*, **7**
- Wu Y., Lin M.-K., Cui C., Krapp L., Lee Y.-N., Youdin A. N., 2024, *ApJ*, **962**, 173
- Youdin A. N., Goodman J., 2005, *ApJ*, **620**, 459
- Yu C., Lai D., 2013, *MNRAS*, **429**, 2748
- Yu C., Li H., 2009, *ApJ*, **702**, 75
- Zebib A., 1987, *Journal of Computational Physics*, **70**, 521
- Zhu Z., Stone J. M., 2014, *ApJ*, **795**, 53
- Zhu Z., Stone J. M., Rafikov R. R., Bai X.-n., 2014, *ApJ*, **785**, 122
- Zsom A., Ormel C. W., Güttler C., Blum J., Dullemond C. P., 2010, *A&A*, **513**, A57
- van der Marel N., et al., 2013, *Science*, **340**, 1199
- van der Marel N., et al., 2021, *AJ*, **161**, 33

APPENDIX A: LINEARIZED EQUATIONS FOR $K_Z \neq 0$

A1 ideal MHD

The linearized continuity equation is

$$\frac{i\Delta\omega}{c_s^2}\delta\Psi - \frac{\partial\delta v_r}{\partial r} - \left[\frac{1}{r} + \frac{1}{L_\rho}\right]\delta v_r - ik_\phi\delta v_\phi - ik_z\delta v_z = 0. \quad (\text{A1})$$

The linearized momentum equations are

$$i\Delta\omega\delta v_r + 2\Omega\delta v_\phi - \frac{\partial\delta\Psi}{\partial r} + \frac{1}{4\pi\rho}\left[i(k_\phi B_\phi + k_z B_z)\delta B_r - \frac{2B_\phi}{r}\delta B_\phi - B_z\frac{\delta B_z}{\partial r} - B_\phi\frac{\delta B_\phi}{\partial r} + \frac{B_\phi^2}{r}\frac{\delta\rho}{\rho}\right] = 0, \quad (\text{A2})$$

$$i\Delta\omega\delta v_\phi - \frac{\kappa^2}{2\Omega}\delta v_r - ik_\phi\delta\Psi + \frac{1}{4\pi\rho}\left[\frac{B_\phi}{r}\delta B_r - ik_\phi B_z\delta B_z + ik_z B_z\delta B_\phi\right] = 0, \quad (\text{A3})$$

$$i\Delta\omega\delta v_z - ik_z\delta\Psi + \frac{1}{4\pi\rho}\left[ik_\phi B_\phi\delta B_z - ik_z B_\phi\delta B_\phi\right] = 0, \quad (\text{A4})$$

The linearized induction equations are

$$i\Delta\omega\delta B_r + i(k_\phi B_\phi + k_z B_z)\delta v_r = 0, \quad (\text{A5})$$

$$i\Delta\omega\delta B_\phi + \left[\frac{\partial v_\phi}{\partial r} - \frac{v_\phi}{r}\right]\delta B_r - B_\phi\frac{\partial\delta v_r}{\partial r} + ik_z[B_z\delta v_\phi - B_\phi\delta v_z] = 0, \quad (\text{A6})$$

$$i\Delta\omega\delta B_z - \frac{B_z}{r}\delta v_r - ik_\phi B_z\delta v_\phi + ik_\phi B_\phi\delta v_z - B_z\frac{\partial\delta v_r}{\partial r} = 0. \quad (\text{A7})$$

A2 non-ideal MHD limit: pure B_ϕ

The non-ideal MHD effects manifest in the induction equations,

$$\begin{aligned} & i\Delta\omega\delta B_r + ik_\phi B_\phi\delta v_r \\ & + \eta_{\text{O}}\left[\frac{\partial^2\delta B_r}{\partial r^2} + \frac{1}{r}\frac{\partial\delta B_r}{\partial r} - (k_\phi^2 + k_z^2)\delta B_r - \frac{\delta B_r}{r^2} - \frac{2}{r}ik_\phi\delta B_\phi\right] \\ & + \eta_{\text{A}}\left[-\frac{\delta B_\phi}{r} - \frac{\partial\delta B_\phi}{\partial r} + ik_\phi\delta B_r\right]ik_\phi \\ & + \eta_{\text{H}}\left[-ik_\phi\delta B_z + ik_z\delta B_\phi\right]ik_\phi \\ & = 0, \end{aligned} \quad (\text{A8})$$

$$\begin{aligned} & i\Delta\omega\delta B_\phi + \left[\frac{\partial v_\phi}{\partial r} - \frac{v_\phi}{r}\right]\delta B_r - B_\phi\frac{\partial\delta v_r}{\partial r} - ik_z B_\phi\delta v_z \\ & + [\eta_{\text{O}} + \eta_{\text{A}}]\left[\frac{\partial^2\delta B_\phi}{\partial r^2} + \frac{1}{r}\frac{\partial\delta B_\phi}{\partial r} - (k_\phi^2 + k_z^2)\delta B_\phi - \frac{\delta B_\phi}{r^2} + \frac{2}{r}ik_\phi\delta B_r\right] \\ & + \eta_{\text{H}}\left[(-ik_z\delta B_r + \frac{\partial\delta B_z}{\partial r})ik_\phi + (-ik_\phi\delta B_z + ik_z\delta B_\phi)\frac{1}{r}\right] \\ & = 0, \end{aligned} \quad (\text{A9})$$

$$\begin{aligned} & i\Delta\omega\delta B_z + ik_\phi B_\phi\delta v_z \\ & + \eta_{\text{O}}\left[\frac{\partial^2\delta B_z}{\partial r^2} + \frac{1}{r}\frac{\partial\delta B_z}{\partial r} - (k_\phi^2 + k_z^2)\delta B_z\right] \\ & + \eta_{\text{A}}\left[-k_\phi^2\delta B_z + k_\phi k_z\delta B_\phi\right] \\ & + \eta_{\text{H}}\left[-\frac{\partial\delta B_\phi}{\partial r} - \frac{\delta B_\phi}{r} + ik_\phi\delta B_r\right]ik_\phi \\ & = 0. \end{aligned} \quad (\text{A10})$$

A3 non-ideal MHD limit: pure B_z

The linearized induction equations are written as

$$\begin{aligned}
& i\Delta\omega\delta B_r + ik_z B_z \delta v_r \\
& + \eta_O \left[\frac{\partial^2 \delta B_r}{\partial r^2} + \frac{1}{r} \frac{\partial \delta B_r}{\partial r} - (k_\phi^2 + k_z^2) \delta B_r - \frac{\delta B_r}{r^2} - \frac{2}{r} ik_\phi \delta B_\phi \right] \\
& + \eta_A \left[-k_z^2 \delta B_r - ik_z \frac{\partial \delta B_z}{\partial r} \right] \\
& + \eta_H \left[-ik_\phi \delta B_z + ik_z \delta B_\phi \right] ik_z \\
& = 0,
\end{aligned} \tag{A11}$$

$$\begin{aligned}
& i\Delta\omega\delta B_\phi + \left[\frac{\partial v_\phi}{\partial r} - \frac{v_\phi}{r} \right] \delta B_r + ik_z B_z \delta v_\phi \\
& + \eta_O \left[\frac{\partial^2 \delta B_\phi}{\partial r^2} + \frac{1}{r} \frac{\partial \delta B_\phi}{\partial r} - (k_\phi^2 + k_z^2) \delta B_\phi - \frac{\delta B_\phi}{r^2} + \frac{2}{r} ik_\phi \delta B_r \right] \\
& + \eta_A \left[k_z k_\phi \delta B_z - k_z^2 \delta B_\phi \right] \\
& + \eta_H \left[-ik_z \delta B_r + \frac{\partial \delta B_z}{\partial r} \right] ik_z \\
& = 0,
\end{aligned} \tag{A12}$$

$$\begin{aligned}
& i\Delta\omega\delta B_z + B_z \left[\frac{1}{L_\rho} \delta v_r - \frac{i\Delta\omega}{c_s^2} \delta \Psi \right] \\
& + [\eta_O + \eta_A] \left[\frac{\partial^2 \delta B_z}{\partial r^2} + \frac{1}{r} \frac{\partial \delta B_z}{\partial r} - (k_\phi^2 + k_z^2) \delta B_z \right] \\
& + \eta_H \left[-\frac{\partial \delta B_\phi}{\partial r} - \frac{\delta B_\phi}{r} + ik_\phi \delta B_r \right] ik_z \\
& = 0.
\end{aligned} \tag{A13}$$

APPENDIX B: SPURIOUS MODES

In a pure B_z field, the ambipolar term in z -component of the induction equation shares the same expression as the resistivity term. Unfortunately, we found that the growth rates of RWI increase indefinitely with k_z for $\text{Am} > 0.2$. This trend persists even at a resolution of $N = 512$ for spectral method. We suspect these modes are spurious and cannot be eliminated by high numerical resolutions. Future studies should focus on addressing this issue.

This paper has been typeset from a $\text{T}_\text{E}\text{X}/\text{L}^\text{A}\text{T}_\text{E}\text{X}$ file prepared by the author.